Core-scale geophysical and hydromechanical analysis of seabed sediments affected by CO_2 venting

By

Ismael Himar Falcon-Suarez[1]*; Anna Lichtschlag[1]; Hector Marin-Moreno[3]; Giorgos Papageorgiou[4,5]; Sourav K. Sahoo[1]; Ben Roche[2]; Ben Callow[2]; Romina A.S. Gehrmann[2]; Mark Chapman[4] & Laurence North[1]

1. National Oceanography Centre, University of Southampton Waterfront Campus. European Way, SO14 3ZH, Southampton, UK.
2. School of Ocean and Earth Science, National Oceanography Centre Southampton, University of Southampton Waterfront Campus, European Way, Southampton SO14 3ZH, UK.
3. Norwegian Geotechnical Institute, PB 3930 Ullevål Stadion, NO-08906 Oslo, Norway.
4. School of Geosciences, University of Edinburgh, Grant Institute, West Mains road, Edinburgh EH9 3FE, UK.
5. Institute of Geoscience and Petroleum, NTNU, S. P. Andersensvei 15A, 7491, Trondheim, Norway.

*Corresponding author: National Oceanography Centre, University of Southampton Waterfront Campus. European Way, SO14 3ZH, Southampton.

Phone: +44 (0)23 8059 6666 Office: 676/07 email: isfalc@noc.ac.uk

Abstract

Safe offshore Carbon Capture Utilization and Storage (CCUS) includes monitoring of the subseafloor, to identify and assess potential CO_2 leaks from the geological reservoir through seal bypass structures. We simulated CO_2-leaking through shallow marine sediments of the North Sea, using two gravity core samples from ~1 and ~2.1 meters below seafloor. Both samples were subjected to brine-CO_2 flow-through, with continuous monitoring of their transport, elastic and mechanical properties, using electrical resistivity, permeability, P-wave velocity and attenuation, and axial strains. We used the collected geophysical data to calibrate a resistivity-saturation model based on Archie's law extended for clay content, and a rock physics for the elastic properties. The P-wave attributes detected the presence of CO_2 in the sediment, but failed in providing accurate estimates of the CO_2 saturation. Our results estimate porosities of 0.44 and 0.54, a background permeability of ~10^{-15} and ~10^{-17} m^2, and maximum CO_2 saturation of 18% and 10% (±5%), for the sandier (shallower) and muddier (deeper) sample, respectively. The finer-grained sample likely suffered some degree of gas-induced fracturing, exhibiting an effective CO_2 permeability increase sharper than the coarser-grained sample. Our core-scale multidisciplinary experiment contributes to improve the general interpretation of shallow sub-seafloor gas distribution and migration patterns.

Key words: elastic waves, electrical resistivity, marine sediments, CO_2 storage

1. Introduction

Carbon Capture Utilization and Storage (CCUS) is a realistic global scale mitigation solution to tackle the excess of CO_2 expelled from industrial production and sequestering it into deep reservoir formations. CO_2 sequestration activities encompasses pre-injection risk assessment about sealing efficiency and mechanical stability of the reservoir, and CO_2 plume migration monitoring during and after CO_2 injection (EU CCS Directive, 2009).

In case of seal failure, the way the CO_2 reaches shallower areas depends on a number of factors, including the porosity and permeability of the overburden formations; sediment heterogeneity and grain size distribution; vertical hydraulic connectivity between layers through existing and induced sedimentary seal bypass systems (Cartwright et al., 2007), such us faults (e.g., Rutqvist, 2012) or chimney structures (e.g., Bull et al., 2018; Karstens and Berndt, 2015; Robinson et al., 2021); and the reactivity of these materials to CO_2 (e.g., Marín-Moreno et al., 2019).

Offshore, gas-escape expressions include seabed depressions known as pockmarks (e.g., Robinson et al., 2021). Most of them are only 2 - 3 m in diameter (Bull et al., 2018), fed by sub-seismic scale structures located at the shallowest part of the sediment column, or by deeper and larger chimney structures with the potential of connecting reservoirs with the seabed (Bull et al., 2018). Hence, the understanding of the hydrodynamic behaviour of sediments prior to venting and pockmark formation is crucial to improve monitoring tools and interpretation of seal bypass systems underground.

In offshore CCUS sites, once the CO_2 reached the seafloor, the detection and quantification of the leak can be done using physicochemical sensors measuring in the water column (e.g., Blackford et al., 2015). However, to minimize the risk of leakage, and for commercial global CO_2 storage operations to become realistic, monitoring CO_2 migration through the sediment column is essential. This is particularly challenging in offshore storage sites, as the deployment of equipment and monitoring require advanced technology (e.g., Robinson et al., 2021). Therefore, understanding the sub-seafloor CO_2 migration patterns is of great importance to inform about best offshore sensors deployment locations, which is critical for setting up the risk assessment for the CCUS complex.

Unlike the sensors used to detect and quantify dissolved CO_2 concentrations and bubbles directly in the water column, inferring the presence of CO_2 below the seafloor requires advanced remote sensing tools. The increase of free gas in the sediment leads to detectable geophysical signatures, as the bulk physical properties of the sediment change. For this reason, active seismic and electromagnetic methods (historically used in reservoir exploration) are the most widespread techniques for CO_2 storage monitoring (e.g., Chadwick et al., 2019; Park et al., 2017). Seismic surveys provide information about the bulk elastic properties of both the mineral skeleton and the pore fluid; electrical datasets complement the seismic interpretation with further complementary information about structure of the porous medium and the fluid(s) distribution therein (e.g., Mavko et al., 2009). Therefore, joint elastic-electrical datasets are powerful tools for reservoir interpretation.

The development of robust tools to identify and interpret the geophysical signatures corresponding to real cases of CO_2 migration from reservoirs through the overburden requires datasets generated from controlled experiments under *in situ* conditions. Field scale physical simulations are challenging, and include pilot site testing (e.g., Michael et al., 2010; Underschultz et al., 2011; Würdemann et al., 2010), and *in situ* release experiments (e.g., Dean et al., 2020; Flohr et al., 2021;

Taylor et al., 2015). Additionally, rock physics flow-through laboratory experiments enable to study the behaviour of CO_2 propagation in (water/brine) saturated porous media in a more controlled manner (Burnside and Naylor, 2014), providing joint elastic-electrical datasets when acoustic and electrical sensors are available (e.g., Alemu et al., 2013; Falcon-Suarez et al., 2017; Kim et al., 2013; Zemke et al., 2010). It is well-known that core-scale laboratory experiments may not be fully representative of the events occurring at field scale. However, they allow the study of specific phenomena to calibrate and improve the understanding of natural processes and interpretation of field scale datasets.

Most of the multiphase-flow laboratory tests for studying elastic and electrical properties of CO_2–bearing porous media focus on the study of the host and sealing formations at CCUS reservoir conditions (generally located at depths greater than 1000 m below seabed). The experimental research of sediments partially saturated with free gas in the shallower part of the sediment column (i.e., the near seafloor sediments) requires a combined petrographic, hydrological, geomechanical and geotechnical approach to complement geophysical data for interpreting seafloor dynamics (e.g., Blouin et al., 2019; Deusner, 2016). But, simulating shallow conditions in the laboratory is challenging. Close to seafloor, the effective stress is low and any increase in pore pressure, e.g., due to the expansion of CO_2 while moving upwards, may affect seafloor stability. Replicating these circumstances in the laboratory requires a precise control of the state of stress and adequate sensors to enable the study of the CO_2–induced hydromechanical effects on the shallower part of the sedimentary column. In May 2019, a controlled *in situ* CO_2-release experiment was conducted in the North Sea (Flohr et al., 2021), funded by the Horizon 2020 project Strategies for Environmental Monitoring of Marine Carbon Capture and

Storage (STEMM-CCS). STEMM-CCS was a multidisciplinary project that aimed to enhance the marine monitoring of CCUS activities to assess the environmental impacts associated with potential CO_2 leaks from the geological reservoir (Dean et al., 2020). A complementary project funded by NERC UK entitled Characterization of Major Overburden Leakage Pathways above Sub-seafloor CO_2 Storage Reservoirs in the North Sea (CHIMNEY (Bull et al., 2018)), focused on improving the understanding of subsurface fluid pathways, and developing tools to identify seal bypass systems and quantify partial gas saturation. During both STEMM-CCS and CHIMNEY several geophysical surveys were carried out in the North Sea (Achterberg and Esposito, 2018; Böttner et al., 2020; Gehrmann et al., 2021; Karstens et al., 2019), including seismic and electromagnetic data acquisition. These geophysical data which together with *in situ* samples and modelling result in a comprehensive amount of information about the shallower part of the sediment column (Robinson et al., 2021).

In this work, we assess the results obtained from laboratory brine-CO_2 flow-through tests with geophysical monitoring, using sediment core samples collected in the vicinity of the Goldeneye platform (Achterberg and Esposito, 2018), nearby the STEMM-CCS CO_2 release experiment site. The aim of the lab tests was to relate geophysical changes in the first 3 metres below seafloor (mbsf) to the observed hydromechanical evolution during the CO_2 injection. Our results contribute to calibrate subseafloor geophysical data collected during the STEMM-CCS CO_2 release experiment and help improve future interpretations of shallow sub-seafloor CO_2 distribution and migration patterns.

2. Methodology

2.1. Core samples information

Gravity core POS527-GC06 was collected prior to the *in situ* CO_2 release experiment close to the experimental release site in the UK sector of the North Sea (POS527 Station 102, latitude, 57 59.734; longitude, 0 22.383 (Achterberg and Esposito, 2018)), containing sediments of the Witch Ground Formation (e.g., Böttner et al., 2020; Roche et al., 2021). Standard international procedures (IODP - international gold standard core curation) were followed to maintain the integrity and minimise water loss of the sediment. The core was cut in 1 m sections and whole rounds were scanned with a multi-sensor core logger (MSCL) at the British Ocean Sediment Core Research Facility (BOSCORF).The MSCL analysis included P-wave velocity (at frequency of 230 kHz), electrical resistivity, bulk density and porosity estimates. After the MSCL analysis the cores sections were split. To preserve the original saturation, the two halves of each core section were wrapped in food grade cling film (and stored at 4° C), which is commonly used as a multilayer barrier film in the food industry. The film has excellent minimal water vapour and oxygen transmission rates, and is transparent making it ideal for core preservation. The grain size of the sediment was determined with a Malvern grain size analyser every 20 cm, and then computed with the program Gradistat (Blott and Pye, 2001), allowing the distinction between sand (grain sizes from 63 – 2,000 μm) and silt (grain sizes from 2 – 63 μm) fractions, expressed in terms of sand:mud ratio in Figure 1. Core permeability was estimated using Hazen's modified and Kozeny-Carman's approximations based on the grain-size percentile 10 (d_{10}), using the equations presented in Rosas et al. (2014) and the fitting parameter β recommended by the same authors for offshore siliciclastic sediments. The inorganic carbon carbonate content of the samples was determined before and after the tests with a ThermoFisher Scientific Flash 2000 Elemental Analyser (EA) by subtracting the organic carbon content, which was measured after the removal of the inorganic carbon with acid, from the total carbon content.

Based on the geophysical and geochemical results (Figure 1), two sample intervals were selected from the core at ~1 and ~2.1 mbsf (hereafter named as samples S-A and S-B, respectively). Samples S-A and S-B were extracted from visually homogeneous areas, weakly laminated, with largest difference in physical properties, and therefore good candidates to study the geophysical variability range in the near-seabed sediments of this part of the Central North Sea. From each interval, a 2 cm length, 5 cm diameter core plug was extracted for this experiment: First, we extracted a ~7 cm subsample of the gravity core sediment from a selected (visually undisturbed) area; then, we drove vertically (along the core axis) a 2 cm length, 5 cm (inner diameter) annulus-wedged mould into the subsample to obtain the test sample plug. The mineralogical composition of the samples was obtained by X-ray diffraction (XRD) with a Philips X'Pert pro XRD-Cu X-ray tube, from trimmings of the gravity core at the sample depths (Table 1). The physical properties of the sediment were changing with depth from sand-dominated at the sediment surface to mud-dominated below 3 mbsf. The two selected samples had a distinctly different grain size (with sand:mud ratio of ~40:60 for sample S-A, and ~25:75 for S-B; Figure 1), and porosities of 0.44 ±0.01, for sample S-A (sandier), and 0.54 ±0.01, for S-B(muddier), with permeabilities (from grain size) in the order of 10^{-14} and 10^{-15} m^2, respectively. Porosities were estimated from core trimmings (collected nearby the samples) using wet-(60° C oven) dry mass balance from well-known soil volume portions, with the estimates being in good agreement with the MSCL data (Figure 1).

The inorganic carbon content was slightly lower in the shallower (1.4 ± 0.3 wt% for S-A) than in the deeper (1.5 ± 0.3 wt% for S-B) sample.

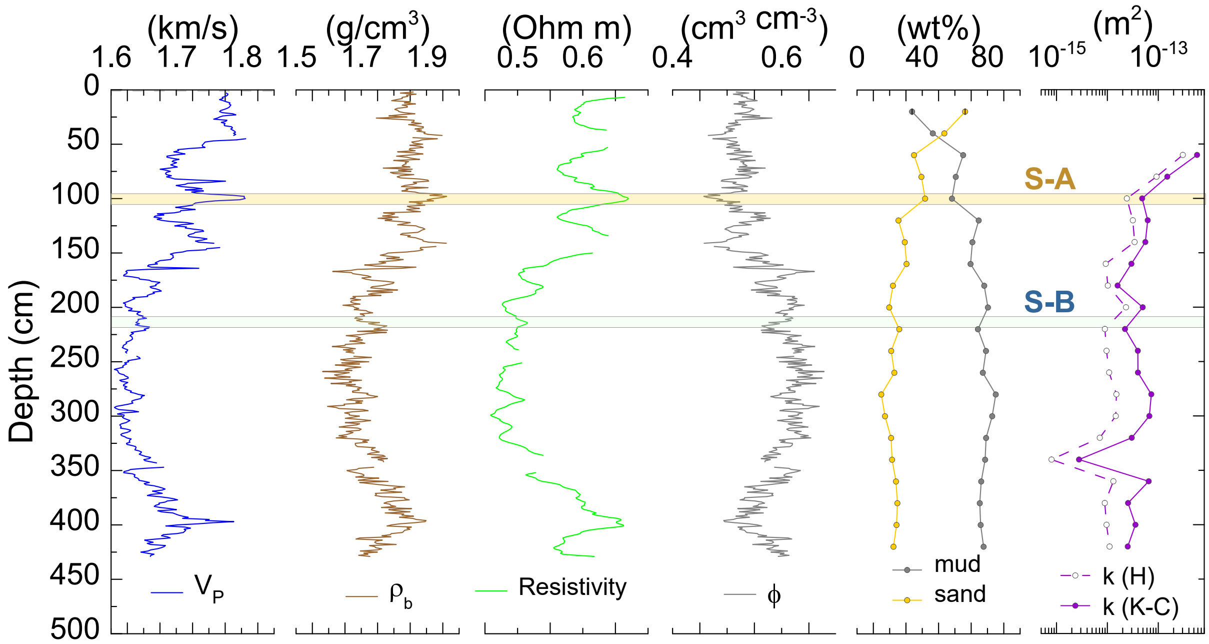

Figure 1. P-wave velocity (V_P at 230 kHz), bulk density (ρ_b), resistivity and porosity (ϕ) obtained from multi-sensor core logger (MSCL at BOSCORF, NOC) analysis along the core POS527-06 (measurements taken every 1 cm depth), estimates of grain size from sampling (in class weight %, every 20 cm depth) and permeability (k) estimates based on grain size percentile 10 using Hazen's (H) and Kozeny-Carman's (K-C) approximations (e.g., Rosas et al., 2014). Marked depths for samples S-A (yellow) and S-B (green).

Table 1. Mineralogical composition (wt%) of the gravity core POS527-GC06, at samples S-A and S-B depths

Depth (cm)	Calcite	Dolomite	Orthoclase	Plagioclase	Quartz	Chlorite	Mica
100	2.7	1.6	6.3	9.9	67.2	5.2	7.1
210	4.3	1.3	8.8	9.9	56.2	6.7	12.7

2.2. Experimental setup

For each sample (S-A and S-B), we performed a brine-CO_2 flow-through test with geophysical and hydromechanical monitoring. The tests were conducted using the high pressure room-temperature (20º C) experimental setup for multiflow-through tests at the National Oceanography Centre, Southampton (NOC) (Falcon-Suarez et al., 2017).

The experimental rig was set up in a multi-flow configuration under well-controlled flow, and confining and pore pressure conditions (ISCO-pumping controllers). We imposed hydrostatic confining conditions of stress for this experiment (i.e., $\sigma_1 = \sigma_2 = \sigma_3$). To minimize fluid-induced corrosiveness effects on the equipment, we use fluid transfer vessels (FTVs) for storing and delivering/receiving the pore fluids. Here, two FTVs were used for delivering brine and CO_2, and a third one for receiving the pore fluid downstream. The rig implements sensors for measuring, simultaneously, ultrasonic P- and S-waves attributes (velocity and attenuation), electrical resistivity and axial strains. Only the ultrasonic sensor for P-wave (transmitting 400 to 1,000 kHz broadband acoustic pulses (Falcon-Suarez et al., 2020b)) provided a reliable signal during this experiment. The sensor is housed in one of the two platens that axially confine the sample through a polyether ether ketone (PEEK) buffer rods. These rods have well-defined acoustic impedance and low energy loss, and provide a delay path with clear top/base sample reflections from which the ultrasonic P-wave velocity (precision ± 0.1%; accuracy ± 0.3%) and attenuation (accuracy ± 5%) are calculated, using the pulse-echo technique (Best, 1992; Falcon-Suarez et al., 2020b). From the axial platens, two arms hold linear variable differential transformer (LVDT) sensors for axial strain monitoring.

Inside the triaxial vessel, an array of 16 stainless steel electrodes are imbibed in the rubber sleeve that isolates the rock sample from the confining mineral oil. Once in contact with the sample, the bulk electrical resistivity is measured using an electrical resistivity tomography (ERT) data acquisition system designed and developed at the NOC (North et al., 2013). The system uses a tetra-polar electrode configuration to minimize electrode polarization artefacts. For any single operational run, the ERT system acquires 208 individual tetra-polar measurements using various permutations of current injection and potential difference sensing electrode pairs. The collected data are then inverted using software based upon EIDORS (Adler and Lionheart, 2006) MATLAB toolkit for both a uniform/homogeneous isotropic resistivity and a heterogeneous isotropic resistivity distribution. Under our experimental P-T-fluid salinity conditions, the error of the resulting resistivity is $<1\%$ for homogenous and isotropic porous media with bulk electrical resistivity $<100\ \Omega$ m (i.e., for the fully saturated, single brine flow stages). Estimation of errors for inhomogeneous and anisotropic resistivity distributions is a non-trivial problem. Indeed, for the case of anisotropic materials no unique solution exists for a resistivity distribution within a body determined from potential measurements made on its surface (Kohn and Vogelius, 1984). Hence, the presence of anisotropy may cause significant errors in resistivity determination. Furthermore the resistivity inverse problem is ill-posed and significant smoothing is usually applied to solution (in this case via a Tikhonov penalty function) to enable solution convergence of the data inversion process. Thus the NOC RPL tomography system is able to detect gross heterogeneity in the internal resistivity distribution of the sample on the order of a centimetre. Also, small high resistivity contrast heterogeneities, for example fractures, are blurred and do not possess sharp boundaries in the interpreted ERT images. Thus while our system can indicate the presence of heterogeneity and or anisotropy its main purpose is to enable the degree of heterogeneity to be assessed. This is useful as ideally one desires the sample to be a representative elementary volume and, therefore, homogeneous (further details about data processing and calibration in North et al. (2013) and North and Best (2014)).

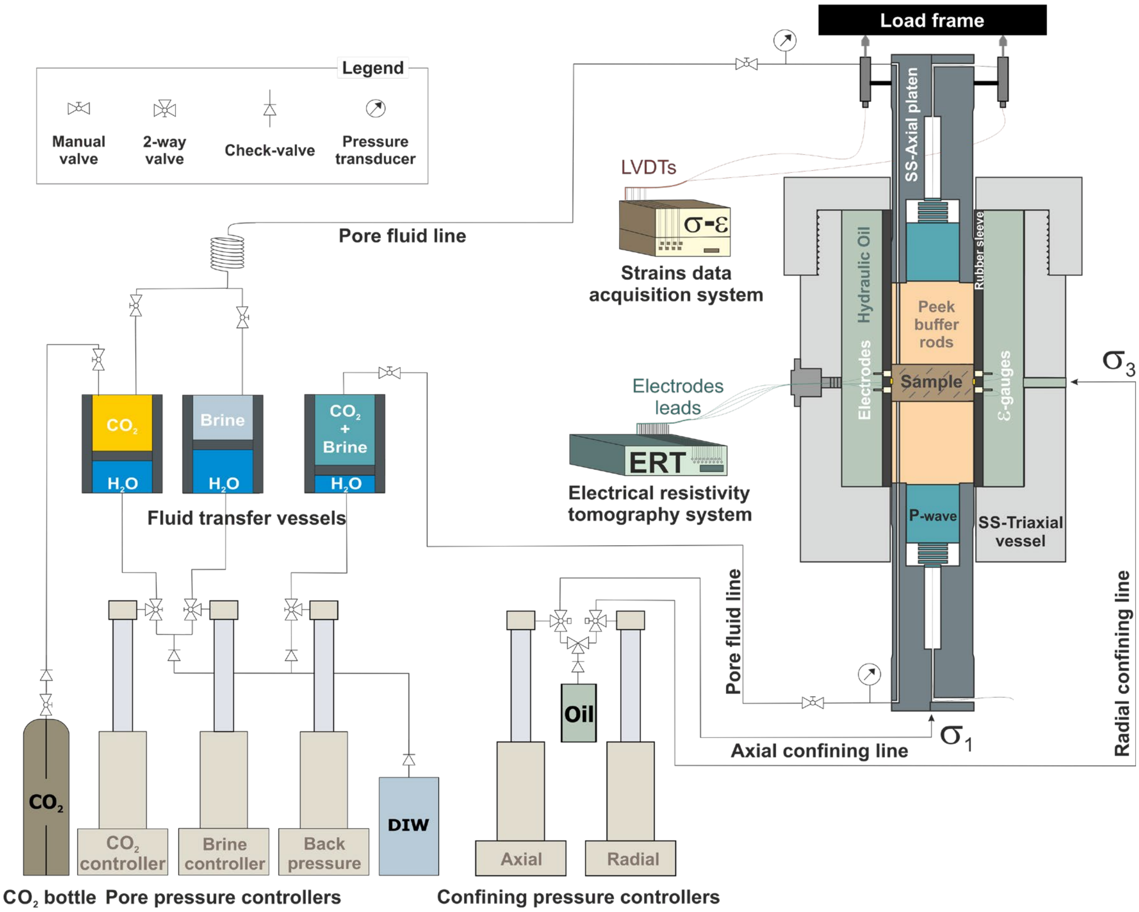

Figure 2. Experimental rig for multi-flow tests at the National Oceanography Centre (NOC), Southampton.

2.3. Brine and CO_2 flow-through (BCFT) tests

The samples are poorly-consolidated and required a careful and special preparation to fit into the triaxial cell of the experimental rig (Figure 2), originally designed to host rock plugs. Originally, we assumed that the samples were still fully saturated in the original seawater brine when tested. This assumption was supported by a posteriori mass balance calculation.

The following procedure was applied to both samples prior to testing:

Firstly, with the sample still placed in the annulus-wedged mould, it was sandwiched by two annuli (PEEK) holding nylon-tight membranes (common pore size < 2 μm), acting as sieves to counteract the unconsolidated state of the sample. This configuration minimizes pipe clogging due to grain migration, and ensures an appropriate top/base repartition of the axial loading (Falcon-Suarez et al., 2018). Also, once the radial stress is slightly increased, the smooth-wall of the two PEEK-annuli in contact with the internal sleeve minimizes potential fluid migration along the sample-sleeve contact.

Secondly, the sample was smoothly removed from the wedge-annulus directly onto the axial platen upstream, and then altogether placed in the triaxial cell core holder at room temperature (20° C). Note that the upstream reservoir (i.e., inlet pipe network) was previously saturated with the testing brine to remove any air in the pipes up to the inlet port. Downstream, the reservoir is left open to remove the air by a continuous brine flow-through upwards, at minimum confining pressure (P_c) of 0.2 MPa.

Thirdly, once the fluid was observed at the outlet port, the hydraulic system was closed and both the confining (P_c) and pore pressure (P_p) were simultaneously increased up to P_c ~1.4 MPa and P_p ~1.2 MPa, the target conditions estimated for the sediments above the STEMM-CCS CO_2-release test site (i.e., 3 mbsf at 120 m water depth (Flohr et al., 2021). Then, the sample was left for no less than 24 h in the triaxial vessel to settle, while subjected to brine flood under minimum flow rate (0.01 mL/min) to enable the testing brine (synthetic 3.5% NaCl aqueous solution, with density 1023.9 kg m^{-3} at the experimental PT conditions) to replace the parental pore fluid.

Our tests combined two consecutive flow-through stages each, consisting of (i) single brine flow and (ii) CO_2 flow-through the brine saturated sample. During the first stage, brine was flushed through the samples and the permeability was calculated using Darcy's law (see below), with slightly variable conditions of effective pressure ($P_{eff} = P_c - P_p$) to assess also the stress-sensitivity of the permeability. For this stage, the system was configured in control pressure mode to avoid negative P_{eff} and development of preferential path-flows, which cause misleading permeability results. In the second stage, the brine saturated sample was flushed with CO_2 (in gas state at the experimental PT conditions, with density 25.6 kg m^{-3}) at increasing flow rates (0.07, 0.18, 0.37, 0.55, 0.74 kg d^{-1}), to investigate the geophysical signatures associated with CO_2-induced hydromechanical changes. With this methodology, we aimed to reproduce an increasing level of hydraulic pressure within the sediment column, similarly to the test procedure used for the STEMM-CCS CO_2 release experiment (Flohr et al., 2021), but under controlled conditions, and at reduced spatial and temporal scale and hydraulic energy.

At the end of the tests, gradually, both P_c and P_p were slowly (~1 h) decreased keeping P_{eff} constant. This procedure minimizes the brine displacement due to CO_2 decompression and gas exolution, in turn, allows a rough estimate (here taken only qualitatively; see below) of the final degree of brine saturation in the sample by mass balance.

2.4. Effective permeability

When more than one fluid is moving through a porous medium, the (effective) permeability of each fluid is different. Our samples are muddy sediments that, under the drainage conditions of our tests, present resistance to gas flow. This resistance is determined by the breakthrough capillary pressure, which is controlled by grain size and pore throats distribution, the properties of the fluids and the flow conditions (Dullien, 1992). . Once the pore pressure exceeds this resistance and the non-wetting phase percolates, the leakage rate (Q_{out}) under laminar (Darcy's flow) conditions is controlled by the effective permeability (k_{eff}) of the system to the breaking fluid flow (CO_2 in our case), as follows:

$$Q_{out}=\frac{A\Delta P_P k_{eff}}{L\mu_{CO2}}, \quad (1)$$

where A and L are area and length of the sample, ΔP_P is the (up- and downstream) pore pressure gradient and μ_{CO2} is the dynamic viscosity of the penetrating fluid (μ_{CO2} = 1.48 x 10^{-5} Pa s^{-1}, at the experimental conditions, i.e., 20 °C and 1.2 MPa). Note that during the first stage of the tests, brine was the only fluid flowing through the sample. Thus, replacing μ_{CO2} by μ_{brine} (1.52 x 10^{-3} Pa s^{-1}, at the experimental conditions) in Eq. (1), k_{eff} provides the absolute permeability to brine (i.e., Darcy's law).

When the two fluids are present in the porous medium, k_{eff} expresses the CO_2 flow-induced (absolute) permeability (k) reduction through the relative permeability to CO_2 ($k_{r,CO2}$) as $k_{eff} = k \times k_{r,CO2}$, with $k_{r,CO2} \in [0, 1]$. $k_{r,CO2}$, and therefore k_{eff}, increases with the partial saturation of CO_2 (i.e., the inverse of brine saturation: $S_{CO2} = 1 - S_w$). Here, we estimate k_{eff} evolution of the two samples during CO_2 flow-through, assuming steady state conditions on the basis of $Q_{in} = Q_{out}$, ΔP_p = constant, and less than 5% variation between two consecutive bulk resistivity measurements (i.e., below resistivity error). However, our k_{eff} estimates provide only apparent values of $k_{r,CO2}$, as we neglected the calculation of the capillary pressure that should be discounted to the experimental value (e.g., Zhang et al., 2017). Our experimental setup is limited to samples with small length-to-diameter factor (~0.4), which leads to uncertainties in terms of pore fluid distribution across the plug due to capillary end effects, affecting the experimental estimate of the capillary pressure. Although the outlet ports have been designed to minimize this effect, we can still expect underestimations of up to one order of magnitude in relative permeability cross-point and 5-10% in saturation (Muñoz-Ibáñez et al., 2019).

2.5. Resistivity into CO_2 saturation

The bulk electrical resistivity increases with the increasing CO_2 content, but also the error associated to the non-uniform distribution of the gas. We use one unique bulk resistivity value for the whole sample to calculate the bulk degree of saturation, adopting the a conservative error of 5% (for the resistivity variability range measured during the experiment (North et al., 2013); see below), for all the values collected after CO_2 injection. The electrical tomography is used to complement our observations with information about the gas distribution patterns.

Resistivity can be transformed into degree of saturation combining Archie's relationships (Archie, 1942) for fully (Eq. (2))and partially saturated (Eq. (3)) granular materials:

$$R_0=R_w\phi^{-m} \tag{2}$$

and

$$R_b=R_wS_w^{-n}a\phi^{-m}, \tag{3}$$

where *R* is the electrical resistivity, with the subscripts *w* for the wet (brine) pore fluid, and *0* and *b* the bulk resistivity of the rock fully and partially saturated, respectively, *a* is an empirical parameter commonly close to unity, ϕ is the porosity fraction contributing to the sample conductivity (net porosity for our unconsolidated none cemented samples), and *m* the cementation exponent. S_w is the degree of brine saturation, with n being the saturation exponent. The saturation exponent depends on the fluid mixture, with accepted values of ~2 for CO_2-brine systems (e.g., Mavko et al., 2009). The cementation exponent of granular seabed sediments varies with the consolidation and fabric, increasing from 1.5 to 1.9 with decreasing grain sphericity and increasing porosity above 0.4 (Jackson et al., 1978) .Combining Eq. (2) and Eq. (3), we can simplify $S_w = (R_o/R_b)^{1/n}$, for a mechanically and chemically invariable porous media.

Archie's relationship is empirical and was initially found valid for clean (shale-free) sandstones. The presence of a shale fraction in the porous media generates additional electrical conductivity pathways along the clay surface that must be corrected (Mavko et al., 2009). The most accepted correction is Waxman–Smits–Juhász model (Juhász, 1981), which accounts for the excess of charges through the charge per unit volume (Q_v), and the increased mobility of ions along the clay surface (B) when in contact with an electrolytic solution (Mavko et al., 2009):

$$S_w=\left(\frac{FR_w}{R_b(1+BQ_vR_w/S_w)}\right)^{1/n}, \tag{4}$$

with the resistivity formation factor $F = a\phi^{-m}$, and

$$B=\frac{-1.28+0.225T-0.4059\cdot 10^{-4}T^2}{1+R_w^{1.23}(0.045T-0.27)}, \tag{5}$$

for temperature (T) in degrees Celsius, and

$$Q_v=\rho_S CEC(1-\phi)/\phi. \tag{6}$$

In the above expression, ρ_s is mineral clay grain density (~2600 kg m^{-3} for chlorite (Mookherjee and Mainprice, 2014)), and CEC the cation exchange capacity ($CEC_{(chorite)}$ = 0.01 meq g^{-1}; (Thomas, 1976)).. The CEC value of our samples can be calculated from their respective mass fractions (x) of chlorite (i.e., CEC = $x_{chlorite}$ x

$CEC_{chlorite}$), as the CEC for the rest of the minerals (Table 1) can be neglected. . With the small clay volume fraction with respect to the pore volume of our samples, the high salinity of the pore water and the low CEC of the chlorite, we anticipate very little contribution of clays to the bulk resistivity in our case, with $Q_{v, S-A}$ = 0.0011 $Q_{v, S-B}$= 0.0015.

2.6. Elastic waves modelling: velocity and attenuation

The porosity for both the shallow sandy sediments we tested, as well as that obtained from the wireline logs, is systematically above the critical porosity assumed for sandstones. Critical porosity (ϕ_c, the largest porosity for which the matrix can support itself without the individual grains being considered a suspension) ranges between 36% - 40% for clean- and up to 45% for clay-rich sandstones (Nur et al., 1998). Then, for the elastic modelling of our clay-rich sand, we require a methodology for calculating the dry properties of samples with porosities above ϕ_c. We not that, despite the porosities of both samples being above the ϕ_c, both samples were self supported and did not behave as suspensions, even at low effective pressure..

Dvorkin et al. (1999) model's has succeded in replicating the elastic properties of near-surface offshore sediments with high porosity. It assumes Hertzian contacts (e.g., Mavko et al., 2009) with partial consolidation around large voids leading to the higher porosity count, assumptions which we adopt here. As a workflow, input parameters for ϕ_c and grain contacts (*n*) are unknown in our case but informed choices consistent with values given in Dvorkin et al. (2001) are ϕ_c =0.36 and grain contacts n=9. However, these should be thought of as tuning parameters rather than inverted values. These values are used together with the knowledge of effective pressure to form Hertz-Mindlin moduli (Mavko et al., 2009), which are then averaged with the grain moduli to produce the predicted dry moduli of the shallow sediment frame. The ambiguity in the grain modulus for a polymineralic rock is compensated by taking the Hill average of the moduli of the individual constituents. We used the average of each mineral bulk (*K*) and shear (*G*) moduli (Table 2) and perform a common Hill average (Mavko et al., 2009) to calculate effective grain moduli. This averaging justifies assuming constant mineralogy for simplicity as the average elastic properties do not change much with depth despite the variation in the individual constituents.

We model the velocity as a function of depth for the log using Gassmann's model (Gassmann, 1951), whose assumptions for a well connected pore space are satisfied in this case (Dvorkin et al., 1999). The porosity and the effective (hydrostatic – lithostatic) pressure are assumed to be functions of depth whereas the remaining parameters, in particular the mineralogy, are assumed constant. Then, we model the partial saturated states using Gassmann's formula and the effective fluid modulus for different fluid distribution scenarios (uniform q = 1, or patchy saturated matrix $q = K_{CO2}/K_{brine}$, with K being the fluid modulus), by means of the patch parameter q in Papageorgiou et al. (2016).

Table 2. Properties and mineralogy used in the modelling of samples A and B (values from Mavko et al. (2009))

	K (GPa)	*G* (GPa)	density (Kg m^{-3})	Reference
Minerals				
Orthoclase	37.5	15	2620	
Plagioclase	75	25	2630	
Calcite	70	30	2700	
Dolomite	70	50	2880	(Mavko et al., 2009) *(Mookherjee and Mainprice, 2014)
Quartz	37	44	2650	
*Chlorite	155	51	2600	
Mica	62	41	2790	

Dry sample				
S-A	0.27	0.36	1456	Hertz-Mindlin moduli
S-B	0.21	0.26	1196	(Mavko et al., 2009)
Fluids				
CO_2	0.05	10^{-7}	25.6	(Span and Wagner, 1996)
Brine	2.39	10^{-7}	1024	(Batzle and Wang, 1992)

Gas propagation trough the brine saturated sediment can be by capillarity or fracture opening (Boudreau, 2012; Roche et al., 2021), with the latter leading to grains displacement and rearrengement.. The amount of CO_2 injected is larger than the solubility limit of CO_2 in brine for our experimental PT and salinity conditions (Duan et al., 2006), and isolate bubbles may form and migrate in our soft and cohesive samples, particularly in our S-B (muddy sample). Hence, we expect gas bubble resonance effects, which would affect both ultrasonic elastic velocity and attenuation. To consider this effect, we also adapt the effective medium rock physics model by Marín-Moreno et al. (2017), initially developed for gas hydrate bearing sediments (e.g., Sahoo et al., 2018; Sahoo et al., 2019), to account for CO_2 gas effects in partially saturated sediments with no hydrate. This model considers frequency-dependent energy disipication due to wave-induced oscillating gas bubbles in a dilute gas-liquid mixture due to viscous, thermal, and inertial (Biot's) properties based on the approach of Smeulders and Van Dongen (1997). This model complements the fluid distribution modelling described above, by providing further information about the way CO_2 bubbles may propagate across the sample.

For the modelling, we use elastic paramerters shown in Table 2, assuming the experimental conditions of effective pressure (0.1 MPa), the pore pressure of the CO_2 when being injected(1.3 MPa) and temperature (20° C).

3. Experimental results and data analysis

3.1. BCFT Tests

Figure 3 shows the geophysical and hydromechanical results of the brine and CO_2 flow-through tests performed on the POS527-GC06 core samples S-A (~1 mbsf, sandier) and S-B (~2.1 mbsf, muddier). Both tests were actively running for ~4.5 h, resulting in ~28 pore volume (PV) throughputs (~4 PV of brine; ~24 PV of CO_2) each.

The permeability during the brine flow stage (i.e., absolute permeability to brine) of both samples is above 10^{-16} m^2, at seafloor conditions. These values are up to two orders of magnitude lower than those estimated theoretically from grain size distributions (Figure 1). This incongruence might be related to the stress sensitivity of the permeability, which is particularly significant for S-B. This effect can be linked to the generation of favourably oriented microcracks, which preferentially appear in fine-grained materials even for very low changes in effective stress (Bolton et al., 2000). The axial strain record also indicates that S-B is more deformable than S-A, although in general terms both samples show very little deformation (<0.01%) at the experimental conditions. Note the permeability at the end of the brine flow stage is obtained at the most realistic state of stress for 1 and 2.1 mbsf (i.e., S-A and S-B), with $k_{S\text{-}A}$ = 2 x 10^{-15} m^2 and $k_{S\text{-}B}$ = 3 x 10^{-17} m^2.

After initiating the CO_2 injection, the differential pore pressure (ΔP_p) suffers sudden increases in both tests (up to 0.2 and 0.07 MPa for S-A and S-B, respectively), which are later gradually recovered. . Then, following these peaks, the pore pressure up- (P_u) increases with the flow rate in the muddier sample (S-B), but not the ΔP_p; while in the sandier sample (S-A), ΔP_p increases with the flow rate. In turn, the k_{eff} increases gradually in S-A (up to 10^{-13} m^2), and abruptly in S-B (up to

10^{-14} m^2), which suggests that the increasing CO_2 flow rate preferentially generated path-flows in the muddier sample. This observation is supported by the little variation in the bulk electrical resistivity for the sample S-B with respect to S-A.

P-wave attributes (velocity, V_P, and attenuation, Q_p^{-1}) are generally very good indicators of both the deformation and pore fluid distribution (e.g., Falcon-Suarez et al., 2017). V_P varies with the confining pressure during the brine flow, inversely following the axial strain trends. Then, in both tests, the arrival of the CO_2, corroborated by a resistivity increase, triggers an initial sharp drop in V_P of ~1%. Thereafter, V_P shows a slight gradual decrease until the end of the tests. Contrarily, Q_P^{-1} is very little affected by changes in the state of stress in both samples, but sharply increases by ~60% when free CO_2 is present in the porous medium.

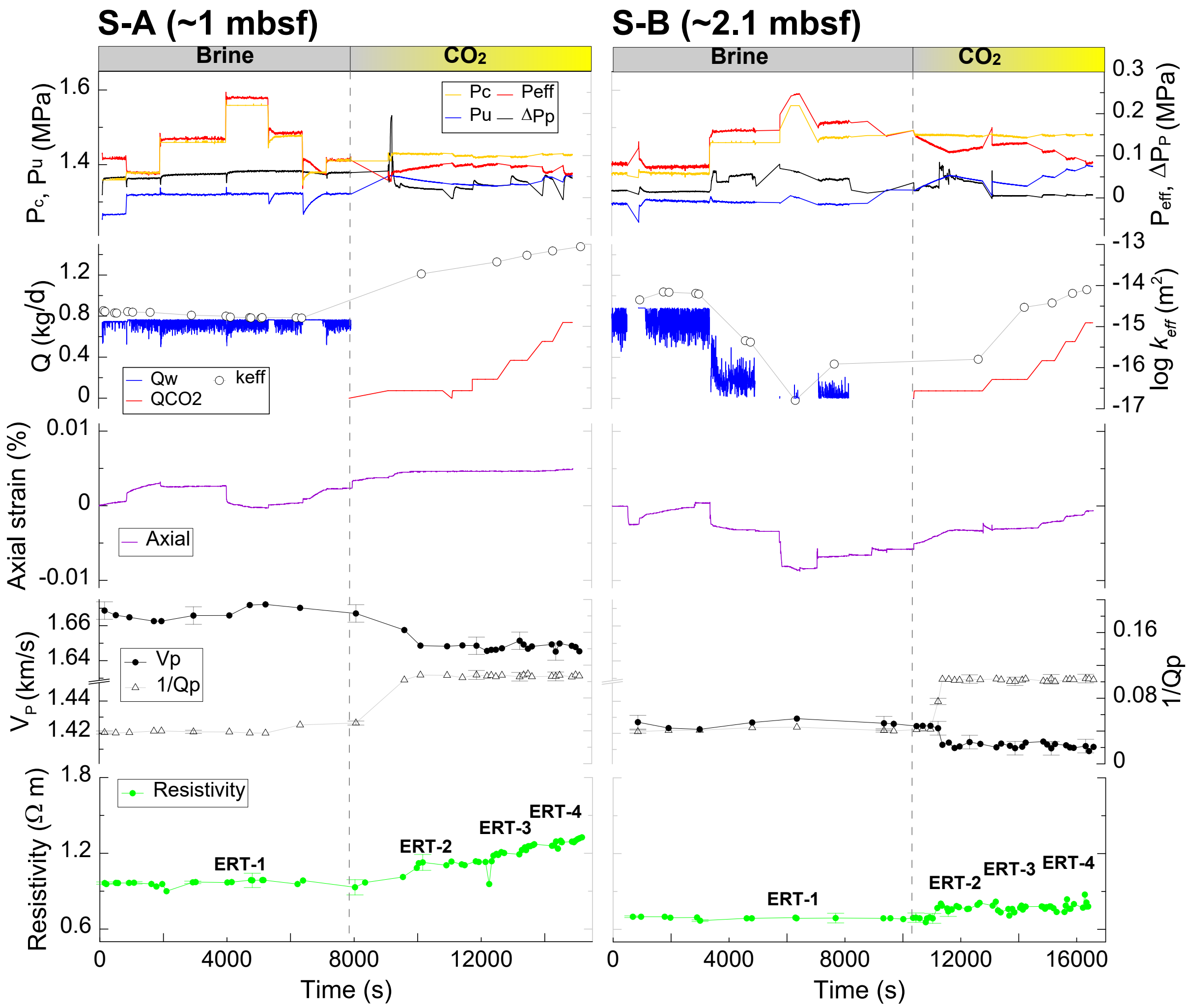

Figure 3. Brine-CO_2 flow-through tests performed on POS527-GC06 core samples S-A (~1 mbsf) and S-B (~2.1 mbsf). P-wave velocities (V_P) and attenuation (Q_P^{-1}), electrical resistivity, axial strains, partial flow rates for CO_2 (Q_{CO2}) and brine (Q_w), confining (P_c), effective (P_{eff}), upstream (P_u) and differential (ΔP_p) pore pressure are plotted together with effective permeability (k_{eff}). The ultrasonic properties were measured at a single frequency of 600 kHz (pulse-echo technique), obtained from Fourier analysis of broad band signals.

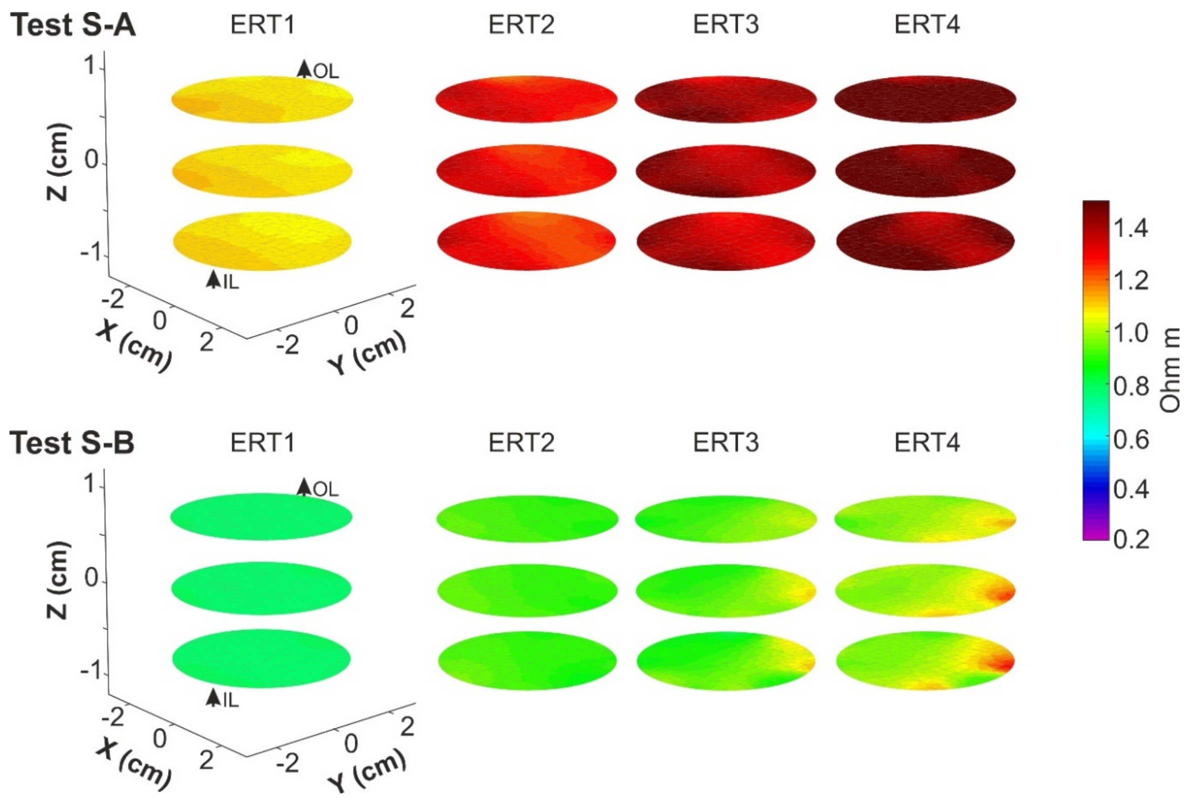

Figure 4. Electrical resistivity tomography of the two samples at different stages of the tests (ERT1 to 4 in Figure 3), represented as three slices of the samples at -0.75, 0 and 0.75 cm height with respect to the sample centre. The dimensions are only represented in the first (left) tomography image, as well as the flow inlet (IL) and outlet (OL) ports, for clarity.

Electrical resistivity is slightly higher in sample S-A. Since both samples were saturated with the same brine, this difference might be associated with the internal grain distribution, heterogeneities and mineral composition (Falcon-Suarez et al., 2020a). ERT images (Figure 4) revel that sample S-B had a more heterogeneous electrical distribution with the increasing CO_2 content, corresponding to the more resistive locations. This observation agrees with previous studies, which suggest that grain size conditions the CO_2 distribution within the sediment, becoming more homogeneous from clay- to sand-rich layers (e.g., Cevatoglu et al., 2015; Roche et al., 2021). The patchy distribution of high electrical resistivity at the lateral of the sample with vertical continuity indicates a preferential channel for CO_2 percolation, with a horizontal section increasing with the flow rate from 5 mm (ERT 3; Q_{CO2} = 0.55 kg d^{-1}) to ~10 mm (ERT4; Q_{CO2} = 0.74 kg d^{-1}).

3.2. Estimation of CO_2 saturation

After each test, the final CO_2 saturation ($S_{CO2,f}$) achieved in each sample was preliminary estimated by mass balance (oven-dried at 60 C), resulting in a $S_{CO2,f}$ ~0.35 for the sample S-A, but $S_{CO2,f}$ ~0.13 for the sample S-B. However, the best fitting curve to the resistivity data led to a $S_{CO2,f}$ of 0.18 ± 0.05 for S-A and 0.09 ± 0.05 for S-B. The adjustment of the empirical parameters *a*, *n*, and *m* (Table 3) in expression (4) was carried out by non-linear least squares from the resistivity data collected during the tests (Figure 3). The CO_2 excess obtained by mass balance in both cases may be linked to brine drainage post-test induced by gas expansion and exolution during the controlled decompression. Despite S-B is a porous medium with higher capillary forces than S-A, it showed a lower CO_2 excess. This contradiction suggests the CO_2 advanced more homogeneously distributed through sample S-A, which agrees with the electrical distribution observations (Figure 4).

Table 3. Fitting parameters for the transformation of resistivity into degree of saturation

Sample	Depth (mbsf)	*a*	*m*	*n*
S-A	1.0	1.04	1.93	1.8
		1.02	1.83	2.0
		1.01	1.78	2.2
S-B	2.1	1.05	1.98	1.8
		1.04	1.94	2
		1.03	1.88	2.2

The resistivity-saturation transformation carries several uncertainties related to the accuracy of our sensors, the effect of the dissolved CO_2, and the potential CO_2-induced porosity changes. Falcon-Suarez et al. (2018) found that the geophysical tools used for this experiment were unable to detect the effect of the dissolved CO_2

on both the bulk resistivity and P-wave velocity under similar T-salinity conditions but higher pressure (i.e., up to three times higher dissolved CO_2, according to Duan et al. (2006)). This is in agreement with Börner et al. (2013), who found that brine salinities as high as the one used here mask effect of dissolved CO_2. In other words, the dissolved CO_2 is below our experimental error, and therefore neglected in our conversion.

The porosity increase associated with the partial dissolution of the carbonate fraction (originally porosity) is an additional source of uncertainty. Reactive transport models suggest these sediments have very low reactivity to CO_2 (Marín-Moreno et al., 2019). According to the dissolution rates observed by Lichtschlag et al. (2021), for this core sample under laboratory conditions (i.e. 20°C and 1 bar), the short time exposure of our samples to CO_2 (~2 h) led to variations of the carbonate content from before to after the tests lying within the uncertainty of the measurement (± 0.3 wt%) in both cases. Therefore, in our resistivity-saturation model, we assume no porosity variations due to dissolution/precipitation processes and no associated changes in brine resistivity.

Figure 5a shows the resistivity-saturation models for S-A and S-B, using the Archie's law modified to account for the effect of clay on the bulk resistivity, while the fitting parameters of the resistivity-saturation model are shown in Table 3.

Then, assuming the brine saturation condition (i.e., S_w = 1), we apply the two models to the core log resistivity data (Figure 5b) to estimate the porosity from expressions (4). For comparison, in Figure 5b we display two additional models considering m = 1.5 and m = 1.9, with a =1 in both cases, to frame the accepted cementation range for high porosity unconsolidated granular sediments (Jackson et al., 1978; Mavko et al., 2009)). As a reference, the former case (i.e., m = 1.5) coincides with that adopted by Gehrmann et al. (2021) to estimate the porosity of the Witch Ground Formation from MSCL resistivity data, while the latter case is closer to that used by Schwalenberg et al. (2020) for the Danube deep-sea fan, Black Sea. The Archie's model for S-A matches better the measured (MSCL) data at lower porosities (i.e., sandier levels), while the S-B one works better for higher porosities (i.e., muddier levels). The upmost part of the sediment column is poorly fitted by high cementation exponents, likely related to an increase of the grain sphericity with the grain size increase upwards (see Figure 1).

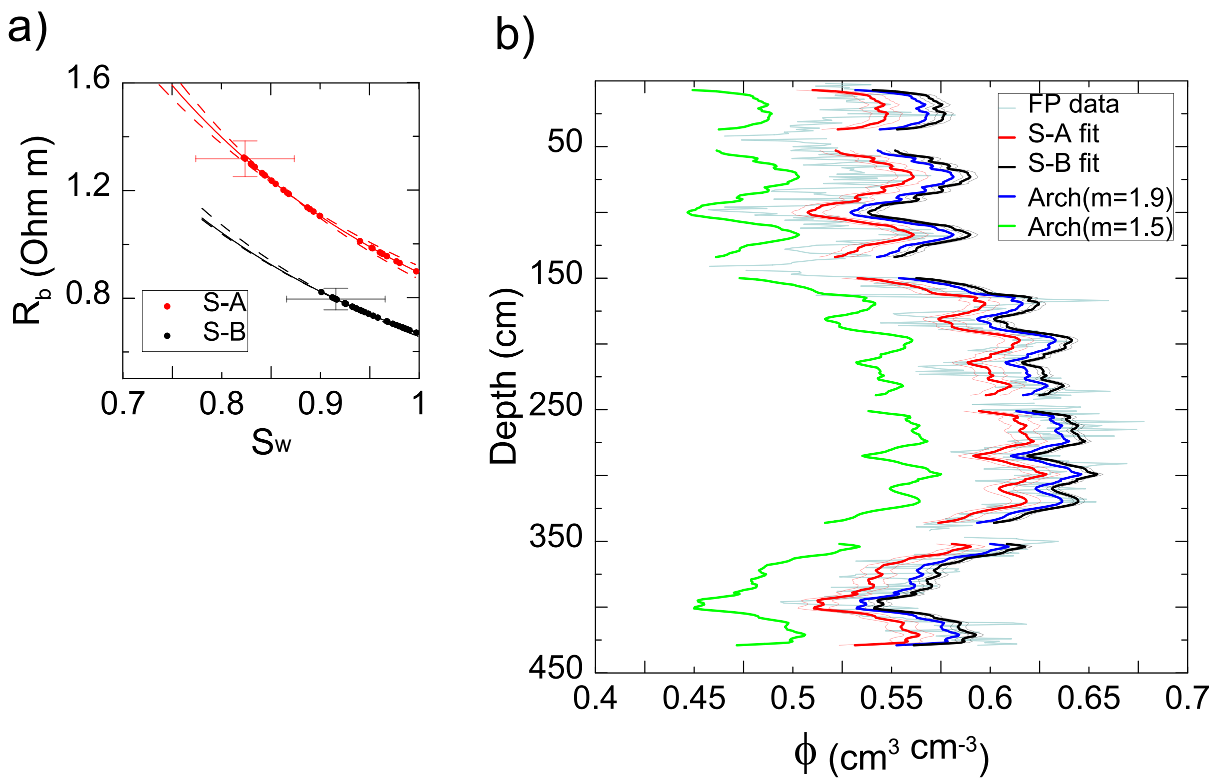

Figure 5. (a) Resistivity into degree of brine saturation applying classic Archie's first and second law accounting for the shale correction (see text for details) for samples S-A and S-B, with dashed lines representing the boundaries associated with ±10% variation in saturation parameter *n.* (b) Porosity variations with depth calculated from the MSCL resistivity data using the Archie's fittings for S-A and S-B, with thin lines representing the boundaries associated with ±10% variation in saturation parameter *n* (see Table 3), and two additional fittings using classic Archie model, adopting m = 1.5 and m = 1.9, respectively, together with the formation porosity data, FP, from MSCL for reference.

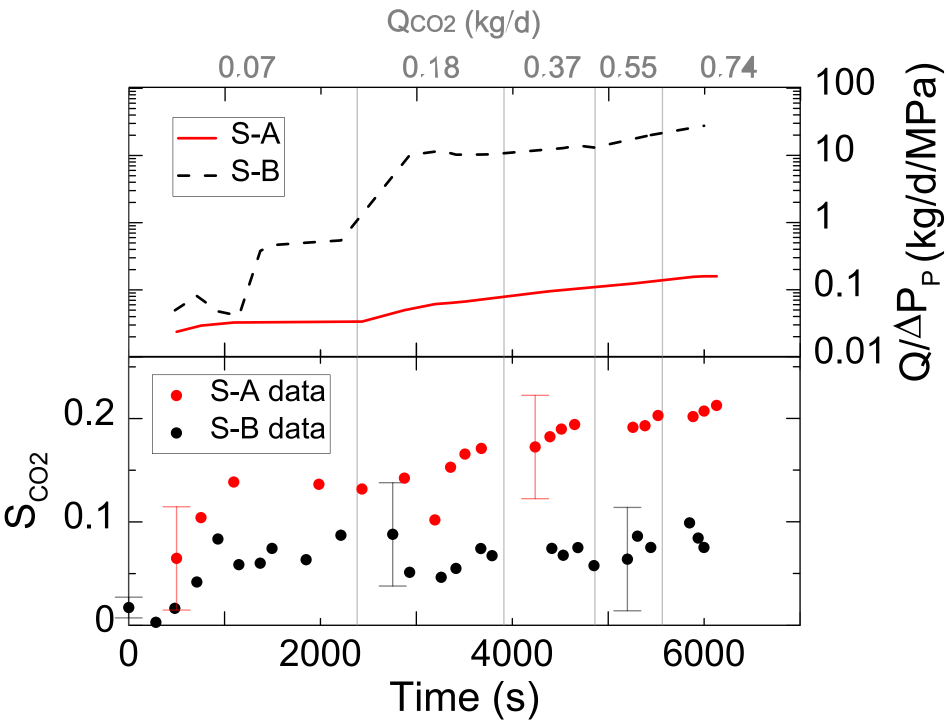

Figure 6. Evolution of the degree of CO_2 saturation (S_{CO2}) and the outlet flow versus differential pore pressure gradient ($Q/\Delta P_p$).. S_{CO2} uncertainties derived from the most conservative error in resistivity (see text).

The CO_2 saturation (S_{CO2}) increases with the increasing CO_2 flowrate during laboratory tests (Figure 6). For sample S-A, the S_{CO2} increases gradually with time, while S-B shows a prompt increase during the first CO_2 injection stage and remain constant afterwards. The $Q/\Delta P_p$ gradient is an indicator of how easy the CO_2 flows through the sample for a given SCO_2 value. This gradient increases gradually with SCO_2, as expected, for S-A; for S-B, the gradient sharply increases, regardless of the SCO_2 that remains constant, which indicates the gradient is still below the threshold value for the flow pathway generated during the first CO_2 flowrate stage. This observation supports the generation of preferential paths for CO_2 flow in sample S-B interpreted from the ERT data.

3.3. Acoustic P-waves

Ultrasonic P-wave velocities (V_P) and attenuations (Q_P^{-1}) vary with the CO_2 content, particularly for S_{CO2} > 0.05 (Figure 7). V_P decreases by 1.1% and 0.8% for S-A and S-B, respectively, while Q_P^{-1} increases by 58% and 63% for S-A and S-B, respectively. V_P variations are very low compared to previous experimental data obtained on reservoir rocks, which report drops above 7% at the arrival of the free-phase CO_2, progressively increasing with S_{CO2} up to above 25% (e.g., Falcon-Suarez et al., 2018; Kim et al., 2013; Kitamura et al., 2014). Q_P^{-1} shows similar values than to previously reported data (e.g., Alemu et al., 2013; Falcon-Suarez et al., 2018), and clearly indicates the arrival of the CO_2 in the pore space; but the quantification of the saturation using Q_P^{-1} may lead to misleading interpretation if fracturing and fluid substitution occur simultaneously (Falcon-Suarez et al., 2020b).

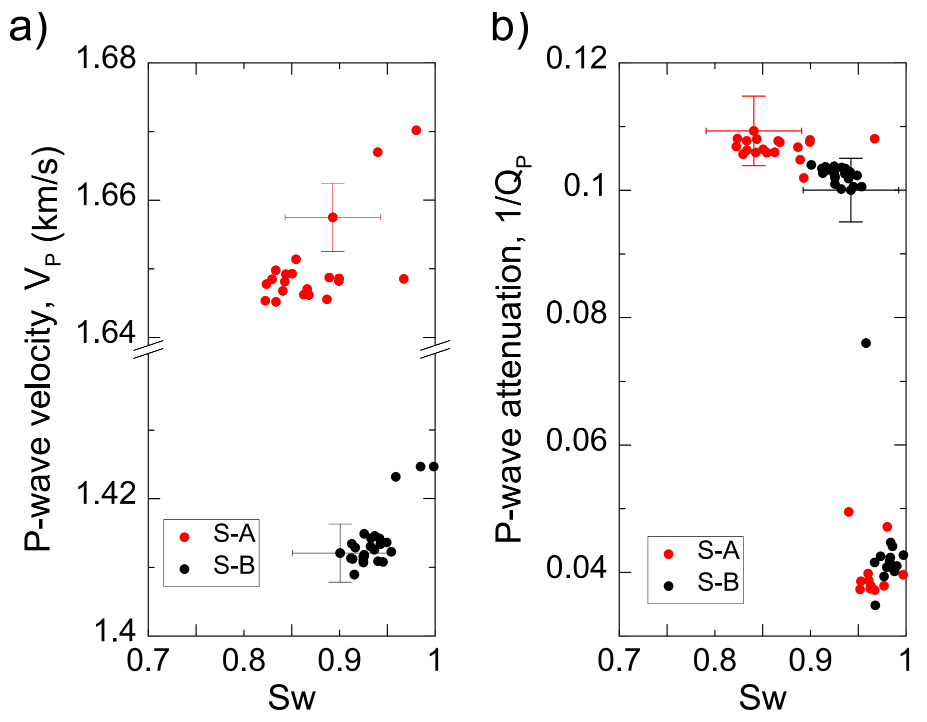

Figure 7. P-wave (a) velocity V_P and (b) attenuation Q_P^{-1} versus degree of brine saturation for the samples S-A and S-B. Only one cross-error bar per sample is displayed for clarity.

Dvorkin et al. (1999)'s model predicts reasonably well the V_P from the MSCL analysis on the gravity core POS527-GC06 below 1.5 mbsf, when considering the S-B mineralogy for the fitting (Figure 8). If the model is based on the S-A mineralogy, the fitting offers good results within the range 1-1.5 mbsf, only. Above 1.5 mbsf, the overestimation of the MSCL data indicates a mineralogical change disregarded by the model, perhaps related to an increment of chlorite. The elastic moduli of chlorite are up to one order of magnitude higher than other clay minerals (e.g., Mavko et al., 2009), and exhibits the greatest moduli among the minerals present in our samples (Table 2). Also chlorite present significant anisotropy, with greater elastic moduli in the direction perpendicular to the basal plane (Mookherjee and Mainprice, 2014), coinciding with the lamination in our case. Note that the MSCL measures V_P perpendicular to the core axis (Geotek, 2016), which in this case is perpendicular to the bedding and therefore aligned with the lower component of the chloride anisotropy. As grain size and sphericity varies upwards, we expect chlorite grains to be more randomly oriented and thus increasing the mean elastic moduli of the minerals. We also predict V_S from this model (Figure 8), although no log data exist to compare it to. However, we anticipate that the shear modulus, therefore the shear velocity, is to some extent overestimated, as it is commonly the case of with assuming Hertzian contacts for high porosity formations (Mavko et al., 2009).

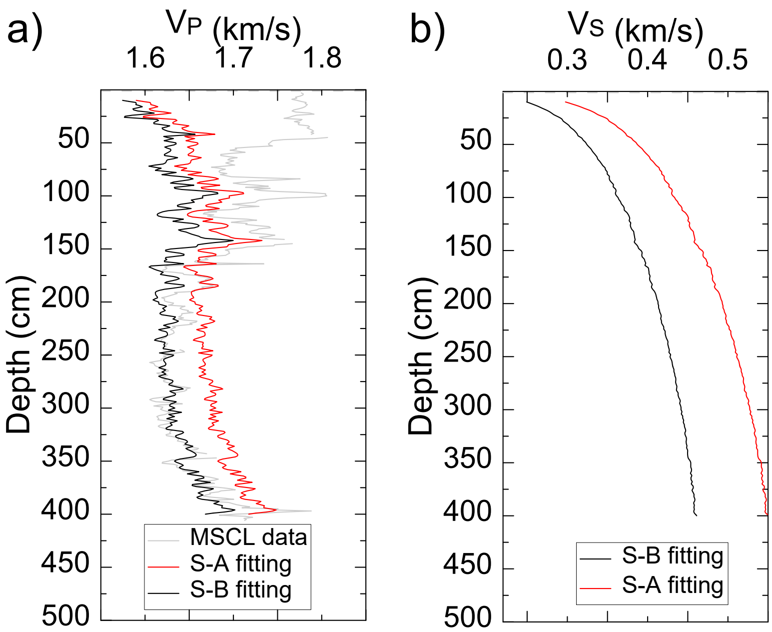

Figure 8. (a) P-wave velocity from MSCL and estimates from the Dvorkin et al. (1999)'s model, and (b) S-wave velocities estimates with depth.

Discrepancies in the absolute values between logging and ultrasonic velocities in our case are related to two opposing effects: the frequency of the measurements and the direction of wave propagation with respect to sediment foliation. V_P increases with frequency for a given material (Batzle et al., 2006); but, for a given frequency V_P decreases with the wave propagation angle with respect to the lamination plane (e.g., Best et al., 2007; Falcon-Suarez et al., 2020a). Our samples present lamination only distinguished by colour gradation, with a bedding thickness in the order of the grain size (i.e., <0.063 mm). From our V_P values and the frequency of measurement (f = 600 kHz), we obtain a wavelength ($\lambda = V_P / f$) of ~2.5 mm. With the wavelength above the bedding thickness, the medium is seen as homogeneous. However, Best et al. (2007) found that thin layering on a scale of less than 0.1 of the wavelength is the dominant cause of velocity and attenuation anisotropy in siltstones and sandstones.

The MSCL velocity (at 230 kHz) should be lower than our ultrasonic one (at 600 kHz), but the former is measured across the core section and therefore parallel to the bedding plane (i.e., fastest V_P component). Conversely, in the flow-through tests we measure the ultrasonic velocity perpendicular to the layering (i.e., slowest V_P component). Comparing the change in velocity with frequency reported by Batzle et al. (2006) and the deviation due to the wave-to-layer orientation reported by Best et al. (2007) or Falcon-Suarez et al. (2020a), we observe the orientation affects more the velocity for the fully saturation case. The orientation impact increases with the layering-induced anisotropy, ultimately conditioned by the microstructure (Falcon-Suarez et al., 2020a), which is presumably more pronounced for sample S-B with a higher clay content (Figure 1). This would explain the higher discrepancy between the MSCL (Figure 8) and ultrasonic measurements for S-B fully (brine) saturated (Figure 9a).

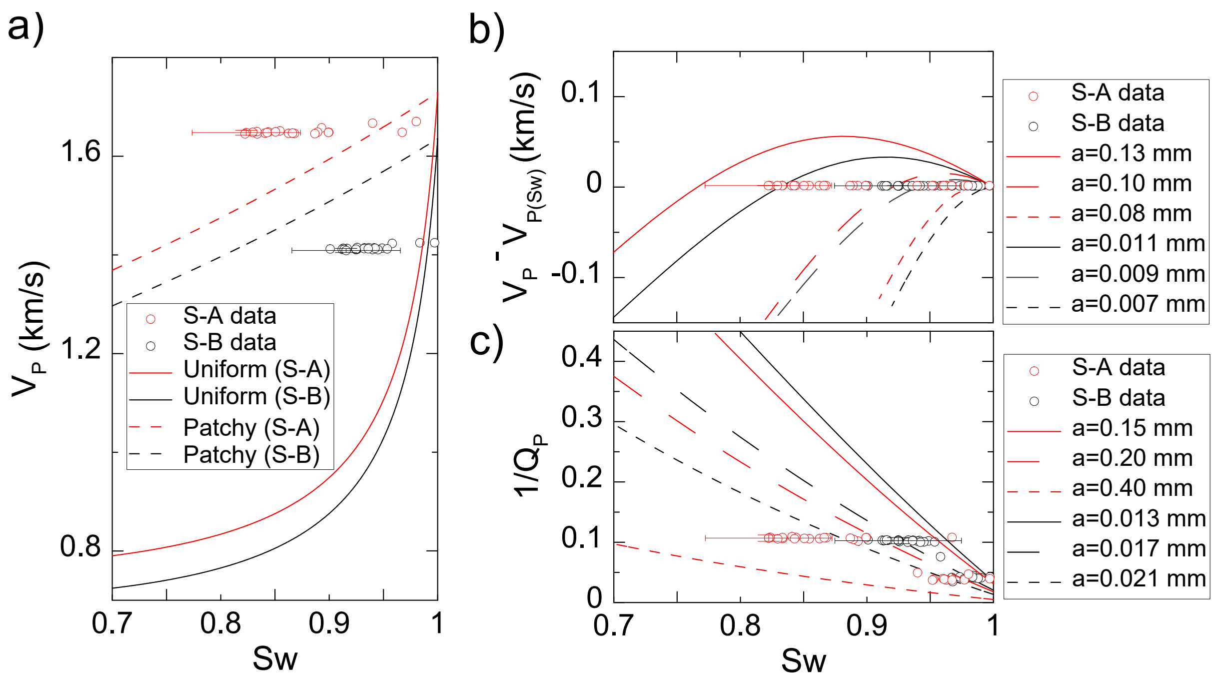

Figure 9. (a) P-wave velocity V_P versus degree of saturation S_w estimates from combining the models of Dvorkin et al. (1999) and Papageorgiou et al. (2016) for the patchy and uniform pore fluid distribution cases. The resonance model of Marín-Moreno et al. (2017) expressing CO_2 bubble size in terms of (b) the P-wave velocity difference with respect to that under fully brine saturation conditions (V_P - $V_{P(Sw)}$) and (c) the P-wave attenuation (Q_P^{-1}) for different bubble radius *a*.

The measured V_P value at full water saturation for sample S-B lies just below the V_P corresponding to the lower Hashin-Shtrikman bound (Figure 9a), calculated in 1.48 km s^{-1} for S-B using the methodology in Berryman (1995), which indicates that the moduli for this sample using the mineralogy of Table 2 are overestimated. The V_P measurement for sample S-A, however, is close to the value predicted by the Dvorkin et al. (1999)'s model when the matrix is fully water saturated (~1.69 km s^{-1}), indicating a higher degree of consolidation but still a poor dependence on CO_2. In this regard, inasmuch as CO_2 induced pathways can be inferred from the heterogeneous resistivity distribution (Figure 4), the elastic modelling considering patchy fluid distribution is more appropriate to explain the results (Figure 9a).

However, our modelling approach for partial saturation is unable to explain the experimental data. These discrepancies might be related to the fact that our model considers homogeneous samples, while our results suggest the decrease in effective pressure during CO_2 injection led to generate some degree of fracturing.

The analysis of the gas bubble resonance effect (Figure 9b,c) shows that, although for both tests the bubble size increases with the CO_2 saturation, the maximum size that explains the data is more than 10 and 100 times smaller than the sample lengths of S-A and S-B, respectively. This observation suggests the preferential path flows consisted of interconnected sub-vertical narrow fractures, with apertures lower than the maximum bubble size, where the CO_2 propagation occurs as a discontinuous gas phase. This propagation would be invisible to the ERT images and therefore it has to be taken hypothetically. The fact that when increasing the saturation a larger radius matches the data better, may imply buble aggregation with the increasing S_{CO2} or CO_2 flowrate. Our results are in similar range as those reported by Choi et al. (2011) for similar sediments and environmental and conditions.

4. Discussion

We found that near-seafloor sediments affected by CO_2 venting can retain CO_2, with greater efficiency in coarser-grained (e.g., sample S-A) layers, despite their lower porosity and larger permeability. Finer-grained (sample S-B like) layers are more sensitive to changes in the effective stress, and prone to develop preferential pathways (fracturing) under similar venting conditions, as previously reported (Deusner, 2016; Robinson et al., 2021). This observation supports the idea that the microstructure of shallow offshore sediment conditions the final stage of the

CO_2 migration from deep geological reservoirs before reaching the water column (Cevatoglu et al., 2015; Roche et al., 2021).

Coarse-grained sediments, with low capillary forces, allows percolation (capillary invasion) and CO_2 partially saturates the sediment; in fine-grained cohesive sediments, the gas propagation causes sediment fracturing by displacing the grains (e.g., Boudreau, 2012). Then, sample S-A was preferentially subjected to capillary invasion as deduced from the increasing CO_2 saturation trend with the injection rate (Figure 6), while the invariable trend for S-B suggests a fracture-dominated regime since very early stages of the test. In this regard, the higher stress-sensitivity of the permeability observed in S-B could be attribute to the presence of cracks existing pre-CO_2 injection, which facilitated the development of CO_2 migration pathways by fracture reopening. Robinson et al. (2021) show cores from the same North Sea area, with similar sediment properties, which contained internal structures that might be acting as precursor discontinuities for fracturing. Induced fracturing hypothesis is also supporting the higher increase of effective permeability for S-B than for S-A, by three and two orders of magnitude relative to the fully saturated background permeability, respectively.

The electrical resistivity tomography confirmed the heterogeneous CO_2 distribution in sample S-B, although the resolution of the tomography is unable to detect minor fracturing. The calculated CO_2 saturation values, ranging from S_{CO2} 0.1 ± 0.05 (S-B) to ~0.18 ± 0.05 (S-A), agree reasonably well with the estimate of S_{CO2} = 0.1 ± 0.03 obtained from the data collected in the field during the STEMM-CCS release experiment (Roche et al., 2021). Roche et al.'s estimate is based on the volumetric positive deformation observed in the seafloor during the release experiment, accounting for the first three metres below the seafloor that combine coarse- and fine-grained layers. Although our results indicate very low sample deformation in both tests, the difference with respect to the values observed in the field is likely related to the higher hydraulic energy used in the latter case (from 8 x 10^{12} m^3 km^2 y^{-1} at the injecting point for the first CO_2 injection step (Flohr et al., 2021)). That hydraulic energy was four orders of magnitude higher than the flow conditions of our lab tests (from 5 x 10^8 m^3 km^2 y^{-1}) .

The potential CO_2-induced crack development in S-A and S-B would be also affecting the interpretation of our ultrasonic measurements, due to fracture features and orientation. Assuming the case of stable fracture propagation in our tests, the fracture length (c) varies within the range 2.5 - 3.0 mm and the elongation is preferentially vertical (Roche et al., 2021). According to our wavelength (λ ~2.5 mm), with $c / \lambda \geq 1$ the medium is seeing as heterogeneous, with the cracks acting as energy scattering fronts (Falcon-Suarez et al., 2020b). Furthermore, when fractures are aligned vertically (i.e., in the direction of the wave propagation), the V_P drop from fully to partially saturated medium (for $S_w > 0.7$) is minimum (Amalokwu et al., 2015; Amalokwu et al., 2017), and the same effect was recently observed in the oblique fractures case (Falcon-Suarez et al., 2020b).

Previous studies show that the gas phase tends to preferentially occupy larger pore cavities (e.g., Muñoz-Ibáñez et al., 2019), which for the case of vertical fractures means that wave propagation between cracks occurs at near fully saturation conditions. This CO_2-induced crack size-elongation combined effect would explain the low velocity and high attenuation changes with the CO_2 arrival. Our ultrasonic data therefore evidence the potential of the P-wave attenuation to infer the presence of CO_2, but at the same time the low sensitivity of this signature for S_{CO2} quantification (i.e., very little variation afterwards). Interestingly, our results are in agreement with the attenuation trend observed in the seismic dataset collected during the STEMM-CCS CO_2 release experiment (Roche et al., 2021).

The small change of V_P in CO_2-brine partially saturated systems containing vertical fractures can be seen from wave frequencies above seismic (f > 200 Hz; (Solazzi et al., 2020)). This observation might affect the identification and interpretation of seal bypass systems with dimensions below seismic resolution, which can even be more effective bypass structures than their larger scale seismic chimneys analogues (Cartwright et al., 2007). In this regard, Waage et al. (2021) found that detectable geophysical signatures of partial CO_2 saturation structures using high-resolution P-Cable 4D seismic method (with f = 500 Hz), highly depends on the pore fluid distribution, with a low detection limit of S_{CO2} ~3% for uniform distribution but up to ~27% if patchy. This S_{CO2}-patchy value is in agreement with our experimental observations, Amalokwu et al. (2017) and Falcon-Suarez et al. (2020b) for sandstones with oriented fractures at ultrasonic frequencies, and can be expected above 200 Hz according to the modelling results reported by Solazzi et al. (2020) if just considering the hypothesis of CO_2-induced sub-vertical fractures.

Our core scale data contribute to the multi-scale and multi-disciplinary characterization required for the understanding of the upper part of fluid scape structures (Robinson et al., 2021), by generating geophysical data related to the hydromechanical response of shallow coarser and finer grained sediments affected by free CO_2 gas migration, in a controlled manner. New rock physics modelling approaches combining dispersion due to gas-induced fracturing near the suspension/cohesion limit might help improve the quantification of gas and fluid phases of seafloor sediments, and the interpretation of pockmarks and fluid scape structures underneath.

5. Summary and conclusions

We have studied the response of shallow sub-seafloor, poorly consolidated sediments to CO_2 gas migration. We have conducted brine-CO_2 flow-through tests with geophysical, hydraulic and mechanical monitoring in the laboratory, using two North Sea seabed sediment samples with different granular distribution. Our data can be used to calibrate geophysical datasets collected during STEMM-CCS and CHIMNEY projects, including the CO_2 release experiment of May 2019 (Flohr et al., 2021), and may help improve the general interpretation of shallow sub-seafloor gas (mainly CO_2 and methane) distribution and migration patterns.

With respect to the geophysical tools we used for CO_2 distribution monitoring, we found that the transformation of resistivity into degree of saturation based on Archie's relationship improves when considering the grain size distribution of the samples. Our ultrasonic P-wave attributes detected the presence CO_2, with the attenuation factor showing clearer signatures; but both fail in providing accurate estimates of the CO_2 saturation.

We found that the permeability of the sediments tested varies from ~10^{-15} m^2 to ~10^{-17} m^2, decreasing with the grain size. When subjected to CO_2 venting at near seabed conditions, these sediments may develop some degree of fracturing, particularly for the finer-grained sediments as evidenced by a sharp increase of the effective CO_2 permeability.

Acknowledgments

The experiment was conducted at the NOC Rock Physics Laboratory in Southampton. We also thank the British Ocean Sediment Core Research Facility

(BOSCORF) for their contribution to this work, and Richard Pearce regarding the XRD analysis.

Funding

We have received funding from the UK's Natural Environment Research Council grants NE/R013535/1 GASRIP and NE/N016041/1 CHIMNEY, and the European Union's Horizon 2020 research and innovation programme grant No. 654462 STEMM-CCS.

References

Achterberg, E.P., Esposito, M., 2018. RV POSEIDON Fahrtbericht / Cruise Report POS527 - Baseline Study for the Environmental Monitoring of Subseafloor CO_2 Storage Operations, in: Report, G. (Ed.), N. Ser. 045, GEOMAR Helmholtz-Zentrum für Ozeanforschung Kiel, Kiel, Germany, p. 90. https://doi.org/10.3289/geomar_rep_ns_45_2018.

Adler, A., Lionheart, W.R.B., 2006. Uses and abuses of EIDORS: an extensible software base for EIT. Physiological Measurement 27, S25-S42. 10.1088/0967-3334/27/5/s03.

Alemu, B.L., Aker, E., Soldal, M., Johnsen, Ø., Aagaard, P., 2013. Effect of sub-core scale heterogeneities on acoustic and electrical properties of a reservoir rock: a CO_2 flooding experiment of brine saturated sandstone in a computed tomography scanner. Geophysical Prospecting 61, 235-250. https://doi.org/10.1111/j.1365-2478.2012.01061.x.

Amalokwu, K., Chapman, M., Best, A.I., Minshull, T.A., Li, X.-Y., 2015. Water saturation effects on P-wave anisotropy in synthetic sandstone with aligned fractures. Geophysical Journal International 202, 1088-1095. https://doi.org/10.1093/gji/ggv192.

Amalokwu, K., Papageorgiou, G., Chapman, M., Best, A.I., 2017. Modelling ultrasonic laboratory measurements of the saturation dependence of elastic modulus: New insights and implications for wave propagation mechanisms. International Journal of Greenhouse Gas Control 59, 148-159. http://dx.doi.org/10.1016/j.ijggc.2017.02.009.

Archie, G.E., 1942. The electrical resistivity log as an aid in determining some reservoir characteristics. Society of Petroleum Engineers. https://doi.org/10.2118/942054-G.

Batzle, M.L., Han, D.-H., Hofmann, R., 2006. Fluid mobility and frequency-dependent seismic velocity-Direct measurements. Geophysics 71, N1-N9. https://doi.org/10.1190/1.2159053.

Batzle, M.L., Wang, Z., 1992. Seismic properties of pore fluids. Geophysics 57, 1396-1408. https://doi.org/10.1190/1.1443207.

Berryman, J.G., 1995. Mixture theories for rock properties. Rock Physics & Phase Relations, 205-228. https://doi.org/10.1029/RF003p0205.

Best, A.I., 1992. The prediction of the reservoir properties of sedimentary rocks from seismic measurements. University of Reading, p. 393.

Best, A.I., Sothcott, J., McCann, C., 2007. A laboratory study of seismic velocity and attenuation anisotropy in near-surface sedimentary rocks. Geophysical Prospecting 55, 609-625. https://doi.org/10.1111/j.1365-2478.2007.00642.x.

Blackford, J., Bull, J.M., Cevatoglu, M., Connelly, D., Hauton, C., James, R.H., Lichtschlag, A., Stahl, H., Widdicombe, S., Wright, I.C., 2015. Marine baseline and monitoring strategies for carbon dioxide capture and storage (CCS). International

Journal of Greenhouse Gas Control 38, 221-229. https://doi.org/10.1016/j.ijggc.2014.10.004.

Blott, S.J., Pye, K., 2001. GRADISTAT: a grain size distribution and statistics package for the analysis of unconsolidated sediments. Earth Surface Processes and Landforms 26, 1237-1248. https://doi.org/10.1002/esp.261.

Blouin, A., Sultan, N., Callot, J.-P., Imbert, P., 2019. Sediment damage caused by gas exsolution: A key mechanism for mud volcano formation. Engineering Geology 263, 105313. https://doi.org/10.1016/j.enggeo.2019.105313.

Bolton, A.J., Maltman, A.J., Fisher, Q., 2000. Anisotropic permeability and bimodal pore-size distributions of fine-grained marine sediments. Marine and Petroleum Geology 17, 657-672. http://dx.doi.org/10.1016/S0264-8172(00)00019-2.

Börner, J.H., Herdegen, V., Repke, J.-U., Spitzer, K., 2013. The impact of CO_2 on the electrical properties of water bearing porous media – laboratory experiments with respect to carbon capture and storage. Geophysical Prospecting 61, 446-460. 10.1111/j.1365-2478.2012.01129.x.

Böttner, C., Haeckel, M., Schmidt, M., Berndt, C., Vielstädte, L., Kutsch, J.A., Karstens, J., Weiß, T., 2020. Greenhouse gas emissions from marine decommissioned hydrocarbon wells: leakage detection, monitoring and mitigation strategies. International Journal of Greenhouse Gas Control 100, 103119. https://doi.org/10.1016/j.ijggc.2020.103119.

Boudreau, B.P., 2012. The physics of bubbles in surficial, soft, cohesive sediments. Marine and Petroleum Geology 38, 1-18. https://doi.org/10.1016/j.marpetgeo.2012.07.002.

Bull, J., Berndt, C., Minshull, T., Henstock, T., Bayrakci, G., Gehrmann, R., Provenzano, G., Bottner, C., Schramm, B., Callow, B., Chapman, M., Birinci, H., Yilo, N., Dewar, M., Chen, B., Saleem, U., Marin-Moreno, H., Lichtschlag, A., Falcon-Suarez, I., Roche, B., James, R.H., Connelly, D.P., Matter, J., Elger, J., Karstens, J., Best, A.I., 2018. Constraining Leakage Pathways Through the Overburden Above Sub-Seafloor CO_2 Storage Reservoirs, 14th Greenhouse Gas Control Technologies Conference (GHGT-14), Melbourne. https://ssrn.com/abstract=3365826.

Burnside, N.M., Naylor, M., 2014. Review and implications of relative permeability of CO_2/brine systems and residual trapping of CO_2. International Journal of Greenhouse Gas Control 23, 1-11. http://doi.org/10.1016/j.ijggc.2014.01.013.

Cartwright, J., Huuse, M., Aplin, A., 2007. Seal bypass systems. AAPG Bulletin 91, 1141-1166. https://doi.org/10.1306/04090705181.

Cevatoglu, M., Bull, J.M., Vardy, M.E., Gernon, T.M., Wright, I.C., Long, D., 2015. Gas migration pathways, controlling mechanisms and changes in sediment acoustic properties observed in a controlled sub-seabed CO_2 release experiment. International Journal of Greenhouse Gas Control 38, 26-43. https://doi.org/10.1016/j.ijggc.2015.03.005.

Chadwick, R.A., Williams, G.A., Falcon-Suarez, I., 2019. Forensic mapping of seismic velocity heterogeneity in a CO_2 layer at the Sleipner CO_2 storage operation, North Sea, using time-lapse seismics. International Journal of Greenhouse Gas Control 90, 102793. https://doi.org/10.1016/j.ijggc.2019.102793.

Choi, J.-H., Seol, Y., Boswell, R., Juanes, R., 2011. X-ray computed-tomography imaging of gas migration in water-saturated sediments: From capillary invasion to conduit opening. Geophysical Research Letters 38. https://doi.org/10.1029/2011GL048513.

Dean, M., Blackford, J., Connelly, D., Hines, R., 2020. Insights and guidance for offshore CO_2 storage monitoring based on the QICS, ETI MMV, and STEMM-CCS projects. International Journal of Greenhouse Gas Control 100, 103120. https://doi.org/10.1016/j.ijggc.2020.103120.

Deusner, C., Gupta, S., Kossel, E., Freise, M., Anbergen, H., Wille, T., Bigalke, N., Haeckel, M. , 2016. The role of high-pressure flow-through experiments for evaluating the mechanical behaviour of gas hydrate-bearing soils, in: F. Wuttke, S.B., & M. Sanchez (Ed.), Energy Geotechnics. CRC Press.

Duan, Z., Sun, R., Zhu, C., Chou, I.M., 2006. An improved model for the calculation of CO_2 solubility in aqueous solutions containing Na^+, K^+, Ca^{2+}, Mg^{2+}, Cl^-, and SO_4^{2-}. Marine Chemistry 98, 131-139. https://doi.org/10.1016/j.marchem.2005.09.001.

Dullien, F.A.L., 1992. Porous Media: Fluid Transport and Pore Structure, 2nd Edition ed. Academic Press Inc., San Diego.

Dvorkin, J., Nur, A., Huffman, A.R., Bowers, G.L., 2001. Critical-Porosity Models, Pressure Regimes in Sedimentary Basins and Their Prediction. American Association of Petroleum Geologists, p. 0.

Dvorkin, J., Prasad, M., Sakai, A., Lavoie, D., 1999. Elasticity of marine sediments: Rock physics modeling. Geophysical Research Letters 26, 1781-1784. https://doi.org/10.1029/1999GL900332.

EU CCS Directive, o.G.S.o.C.D., 2009. DIRECTIVE 2009/31/EC OF THE EUROPEAN PARLIAMENT AND OF THE COUNCIL, Official Journal of the European Union p. L 140/114 EN. https://eur-lex.europa.eu/LexUriServ/LexUriServ.do?uri=OJ:L:2009:140:0114:0135:EN:PDF.

Falcon-Suarez, I., Marín-Moreno, H., Browning, F., Lichtschlag, A., Robert, K., North, L.J., Best, A.I., 2017. Experimental assessment of pore fluid distribution and geomechanical changes in saline sandstone reservoirs during and after CO_2 injection. International Journal of Greenhouse Gas Control 63, 356-369. https://doi.org/10.1016/j.ijggc.2017.06.019.

Falcon-Suarez, I., Papageorgiou, G., Chadwick, A., North, L., Best, A., Chapman, M., 2018. CO_2-brine flow-through on an Utsira Sand core sample: Experimental and modelling. Implications for the Sleipner storage field. International Journal of Greenhouse Gas Control 68, 236-246. https://doi.org/10.1016/j.ijggc.2017.11.019.

Falcon-Suarez, I.H., North, L., Callow, B., Bayrakci, G., Bull, J., Best, A., 2020a. Experimental assessment of the stress-sensitivity of combined elastic and electrical anisotropy in shallow reservoir sandstones. Geophysics 85, MR271. https://doi.org/10.1190/geo2019-0612.1.

Falcon-Suarez, I.H., Papageorgiou, G., Jin, Z., Muñoz-Ibáñez, A., Chapman, M., Best, A.I., 2020b. CO_2-brine substitution effects on ultrasonic wave propagation through sandstone with oblique fractures. Geophysical Research Letters 47, e2020GL088439. https://doi.org/10.1029/2020GL088439.

Flohr, A., Schaap, A., Achterberg, E.P., Alendal, G., Arundell, M., Berndt, C., Blackford, J., Böttner, C., Borisov, S.M., Brown, R., Bull, J.M., Carter, L., Chen, B., Dale, A.W., de Beer, D., Dean, M., Deusner, C., Dewar, M., Durden, J.M., Elsen, S., Esposito, M., Faggetter, M., Fischer, J.P., Gana, A., Gros, J., Haeckel, M., Hanz, R., Holtappels, M., Hosking, B., Huvenne, V.A.I., James, R.H., Koopmans, D., Kossel, E., Leighton, T.G., Li, J., Lichtschlag, A., Linke, P., Loucaides, S., Martínez-Cabanas, M., Matter, J.M., Mesher, T., Monk, S., Mowlem, M., Oleynik, A., Papadimitriou, S., Paxton, D., Pearce, C.R., Peel, K., Roche, B., Ruhl, H.A., Saleem, U., Sands, C., Saw, K., Schmidt, M., Sommer, S., Strong, J.A., Triest, J., Ungerböck, B., Walk, J., White, P., Widdicombe, S., Wilson, R.E., Wright, H., Wyatt, J., Connelly, D., 2021. Towards improved monitoring of offshore carbon storage: A real-world field experiment detecting a controlled sub-seafloor CO2 release. International Journal of Greenhouse Gas Control 106, 103237. https://doi.org/10.1016/j.ijggc.2020.103237.

Gassmann, F., 1951. Elastic waves through a packing of spheres. Geophysics 16, 673-685. https://doi.org/10.1190/1.1437718.

Gehrmann, R.A.S., Provenzano, G., Bottner, C., Marin-Moreno, H., Bayrakci, G., Tan, Y.Y., Naima K. Yilo, Weitemeyer, K.A., Minshull, T.A., Bull, J.M., Berndt, C., 2021. Porosity and free gas estimates from controlled source electromagnetic data at the Scanner Pockmark in the North Sea. Submitted for publication.

Geotek, 2016. Multi-Sensor Core Logger - Manual. https://www.geotek.co.uk/wp-content/uploads/2016/04/MSCL-manual-1-Nov-16.pdf.

Jackson, P.D., Smith, D.T., Stanford, P.N., 1978. Resistivity-porosity-particle shape relationships for marine sands. GEOPHYSICS 43, 1250-1268. 10.1190/1.1440891.

Juhász, I., 1981. Normalised Qv - The ky to shaly sand evaluation using the Waxman-Smits equation in the absence of core data, SPWLA 22nd Annual Logging Symposium. Society of Petrophysicists and Well-Log Analysts, Mexico City, Mexico, p. 36.

Karstens, J., Berndt, C., 2015. Seismic chimneys in the Southern Viking Graben – Implications for palaeo fluid migration and overpressure evolution. Earth and Planetary Science Letters 412, 88-100. https://doi.org/10.1016/j.epsl.2014.12.017.

Karstens, J., Böttner, C., Edwards, M., Falcon-Suarez, I., Flohr, A., James, R., Lichtschlag, A., Maicher, D., Pheasant, I., Roche, B., Schramm, B., Wilson, M., 2019. RV MARIA S. MERIAN Fahrtbericht / Cruise Report MSM78 - PERMO 2, Edinburgh – Edinburgh (U.K.), 16.10. – 25.10.2018, in: Report, G. (Ed.), N. Ser. 048, GEOMAR Helmholtz-Zentrum für Ozeanforschung Kiel, Kiel, Germany, p. 60. https://doi.org/10.3289/geomar_rep_ns_48_2019.

Kim, J., Nam, M.J., Matsuoka, T., 2013. Estimation of CO_2 saturation during both CO_2 drainage and imbibition processes based on both seismic velocity and electrical resistivity measurements. Geophysical Journal International 195, 292-300. https://doi.org/10.1093/gji/ggt232.

Kitamura, K., Xue, Z., Kogure, T., Nishizawa, O., 2014. The potential of Vs and Vp–Vs relation for the monitoring of the change of CO_2-saturation in porous sandstone. International Journal of Greenhouse Gas Control 25, 54-61. http://dx.doi.org/10.1016/j.ijggc.2014.03.013.

Kohn, R., Vogelius, M., 1984. Determining conductivity by boundary measurements. Communications on Pure and Applied Mathematics 37, 289-298. https://doi.org/10.1002/cpa.3160370302.

Lichtschlag, A., Haeckel, M., Olierook, D., Peel, K., Flohr, A., Pearce, C.R., James, R.H., Marieni, C., Connelly, D.P., 2021. Impact of CO2 leakage from sub-seabed carbon dioxide storage on sediment and porewater geochemistry. International Journal of Greenhouse Gas Control This issue, Submitted for publication.

Marín-Moreno, H., Bull, J.M., Matter, J.M., Sanderson, D.J., Roche, B.J., 2019. Reactive transport modelling insights into CO_2 migration through sub-vertical fluid flow structures. International Journal of Greenhouse Gas Control 86, 82-92. https://doi.org/10.1016/j.ijggc.2019.04.018.

Marín-Moreno, H., Sahoo, S.K., Best, A.I., 2017. Theoretical modeling insights into elastic wave attenuation mechanisms in marine sediments with pore-filling methane hydrate. Journal of Geophysical Research: Solid Earth 122, 1835-1847. https://doi.org/10.1002/2016jb013577.

Mavko, G., Mukerji, T., Dvorkin, J., 2009. Rock physics handbook - Tools for seismic analysis in porous media. Cambridge University Press, New York.

Michael, K., Golab, A., Shulakova, V., Ennis-King, J., Allinson, G., Sharma, S., Aiken, T., 2010. Geological storage of CO_2 in saline aquifers: A review of the experience from existing storage operations. International Journal of Greenhouse Gas Control 4, 659-667. http://doi.org/10.1016/j.ijggc.2009.12.011.

Mookherjee, M., Mainprice, D., 2014. Unusually large shear wave anisotropy for chlorite in subduction zone settings. Geophysical Research Letters 41, 1506-1513. https://doi.org/10.1002/2014GL059334.

Muñoz-Ibáñez, A., Falcon-Suarez, I.H., Marín-Moreno, H., Martín, J.D., Mackin, P., 2019. Transport properties of saline CO_2 storage reservoirs with unconnected fractures from brine-CO_2 flow-through tests. Journal of Petroleum Science and Engineering, 106551. https://doi.org/10.1016/j.petrol.2019.106551.

North, L., Best, A.I., Sothcott, J., MacGregor, L., 2013. Laboratory determination of the full electrical resistivity tensor of heterogeneous carbonate rocks at elevated pressures. Geophysical Prospecting 61, 458-470. https://doi.org/10.1111/j.1365-2478.2012.01113.x.

North, L.J., Best, A.I., 2014. Anomalous electrical resistivity anisotropy in clean reservoir sandstones. Geophysical Prospecting 62, 1315-1326. 10.1111/1365-2478.12183.

Nur, A., Mavko, G., Dvorkin, J., Galmudi, D., 1998. Critical porosity: A key to relating physical properties to porosity in rocks. The Leading Edge 17, 357-362. https://doi.org/10.1190/1.1437977.

Papageorgiou, G., Amalokwu, K., Chapman, M., 2016. Theoretical derivation of a Brie-like fluid mixing law. Geophysical Prospecting 64, 1048-1053. https://doi.org/10.1111/1365-2478.12380.

Park, J., Guillaume, S., Vöge, M., 2017. 2.5D inversion and joint interpretation of CSEM data at Sleipner CO_2 storage. Energy Procedia 114, 3989 – 3996. https://doi.org/10.3997/2214-4609.201602173.

Robinson, A.H., Callow, B., Böttner, C., Yilo, N., Provenzano, G., Falcon-Suarez, I.H., Marín-Moreno, H., Lichtschlag, A., Bayrakci, G., Gehrmann, R., Parkes, L., Roche, B., Saleem, U., Schramm, B., Waage, M., Lavayssière, A., Li, J., Jedari-Eyvazi, F., Sahoo, S., Deusner, C., Kossel, E., Minshull, T.A., Berndt, C., Bull, J.M., Dean, M., James, R.H., Chapman, M., Best, A.I., Bünz, S., Chen, B., Connelly, D.P., Elger, J., Haeckel, M., Henstock, T.J., Karstens, J., Macdonald, C., Matter, J.M., North, L., Reinardy, B., 2021. Multiscale characterisation of chimneys/pipes: Fluid escape structures within sedimentary basins. International Journal of Greenhouse Gas Control 106, 103245. https://doi.org/10.1016/j.ijggc.2020.103245.

Roche, B., Bull, J.M., Marin-Moreno, H., Leightond, T., Falcon-Suarez, I.H., White, P.R., Provenzano, G., Tholen, M., Lichtschlag, A., Lid, J., Faggetter, M., 2021. Time-lapse imaging of CO_2 migration within near-surface sediments during a controlled sub-seabed release experiment. International Journal of Greenhouse Gas Control, Submitted for publication.

Rosas, J., Lopez, O., Missimer, T.M., Coulibaly, K.M., Dehwah, A.H.A., Sesler, K., Lujan, L.R., Mantilla, D., 2014. Determination of Hydraulic Conductivity from Grain-Size Distribution for Different Depositional Environments. Groundwater 52, 399-413. https://doi.org/10.1111/gwat.12078.

Rutqvist, J., 2012. The geomechanics of CO_2 storage in deep sedimentary formations. Geotechnical and Geological Engineering 30, 525-551. http://doi.org/10.1007/s10706-011-9491-0.

Sahoo, S.K., Madhusudhan, B.N., Marín-Moreno, H., North, L.J., Ahmed, S., Falcon-Suarez, I.H., Minshull, T.A., Best, A.I., 2018. Laboratory insights into the effect of sediment-hosted methane hydrate morphology on elastic wave velocity from time-lapse 4-D synchrotron X-ray computed tomography. Geochemistry, Geophysics, Geosystems 19, 4502– 4521. https://doi.org/10.1029/2018GC007710.

Sahoo, S.K., North, L.J., Marín-Moreno, H., Minshull, T.A., Best, A.I., 2019. Laboratory observations of frequency-dependent ultrasonic P-wave velocity and attenuation during methane hydrate formation in Berea sandstone. Geophysical Journal International 219, 713-723. https://doi.org/10.1093/gji/ggz311.

Schwalenberg, K., Gehrmann, R.A.S., Bialas, J., Rippe, D., 2020. Analysis of marine controlled source electromagnetic data for the assessment of gas hydrates in the Danube deep-sea fan, Black Sea. Marine and Petroleum Geology 122, 104650. https://doi.org/10.1016/j.marpetgeo.2020.104650.

Smeulders, D.M.J., Van Dongen, M.E.H., 1997. Wave propagation in porous media containing a dilute gas–liquid mixture: theory and experiments. Journal of Fluid Mechanics 343, 351-373. https://doi.org/10.1017/S0022112097005983.

Solazzi, S.G., Hunziker, J., Caspari, E., Rubino, J.G., Favino, M., Holliger, K., 2020. Seismic signatures of fractured porous rocks: The partially saturated case. Journal of Geophysical Research: Solid Earth 125, e2020JB019960. https://doi.org/10.1029/2020jb019960.

Span, R., Wagner, W., 1996. A new equation of state for carbon dioxide covering the fluid region from the triple-point temperature to 1100 K at pressures up to 800 MPa. Journal of Physical and Chemical Reference Data 25, 1509-1596. http://dx.doi.org/10.1063/1.555991.

Taylor, P., Stahl, H., Vardy, M.E., Bull, J.M., Akhurst, M., Hauton, C., James, R.H., Lichtschlag, A., Long, D., Aleynik, D., Toberman, M., Naylor, M., Connelly, D., Smith, D., Sayer, M.D.J., Widdicombe, S., Wright, I.C., Blackford, J., 2015. A novel sub-seabed CO_2 release experiment informing monitoring and impact assessment for geological carbon storage. International Journal of Greenhouse Gas Control 38, 3-17. https://doi.org/10.1016/j.ijggc.2014.09.007.

Thomas, E.C., 1976. The Determination of Qv From Membrane Potential Measurements on Shaly Sands. Journal of Petroleum Technology 28, 1087-1096. 10.2118/5505-pa.

Underschultz, J., Boreham, C., Dance, T., Stalker, L., Freifeld, B., Kirste, D., Ennis-King, J., 2011. CO_2 storage in a depleted gas field: An overview of the CO2CRC Otway Project and initial results. International Journal of Greenhouse Gas Control 5, 922-932. https://doi.org/10.1016/j.ijggc.2011.02.009.

Waage, M., Singhroha, S., Bünz, S., Planke, S., Waghorn, K.A., Bellwald, B., 2021. Feasibility of using the P-Cable high-resolution 3D seismic system in detecting and monitoring CO2 leakage. International Journal of Greenhouse Gas Control 106, 103240. https://doi.org/10.1016/j.ijggc.2020.103240.

Würdemann, H., Möller, F., Kühn, M., Heidug, W., Christensen, N.P., Borm, G., Schilling, F.R., 2010. CO2SINK—From site characterisation and risk assessment to monitoring and verification: One year of operational experience with the field laboratory for CO_2 storage at Ketzin, Germany. International Journal of Greenhouse Gas Control 4, 938-951. https://doi.org/10.1016/j.ijggc.2010.08.010.

Zemke, K., Liebscher, A., Wandrey, M., 2010. Petrophysical analysis to investigate the effects of carbon dioxide storage in a subsurface saline aquifer at Ketzin, Germany (CO2SINK). International Journal of Greenhouse Gas Control 4, 990-999. https://doi.org/10.1016/j.ijggc.2010.04.008.

Zhang, Y., Nishizawa, O., Park, H., Kiyama, T., Lei, X., Xue, Z., 2017. The Pathway-Flow Relative Permeability of CO2: Measurement by Lowered Pressure Drops. Water Resources Research 53, 8626-8638. https://doi.org/10.1002/2017wr020580.